Available online at www.sciencedirect.com
SCIENCE DIRECT®
NDT&E International 36 (2003) 523–533
NDT&E international
www.elsevier.com/locate/ndteint

Near field inversion method to measure the material properties of a layer

J. Christian Stolzenburg[a,1], John W. Doane[b], Jacek Jarzynski[c], Laurence J. Jacobs[a,c,*]

[a]School of Civil and Environmental Engineering, Georgia Institute of Technology, Atlanta, GA 30332, USA
[b]Georgia Tech Research Institute (GTRI-SEAL), Georgia Institute of Technology, Atlanta, GA 30332, USA
[c]G.W. Woodruff School of Mechanical Engineering, Georgia Institute of Technology, Atlanta, GA 30332, USA

Received 22 December 2002; revised 3 March 2003; accepted 15 March 2003

Abstract

This study develops an in situ methodology that uses ultrasonic waves to measure the material properties of a layer. These material properties include the longitudinal and shear wave speeds, as well as the thickness of the layer. The unknown properties are determined by comparing measured experimental data with values obtained from a theoretical model. Emphasis is placed on the effectiveness of measuring both the in-plane, and the out-of-plane surface displacement components with a laser Doppler vibrometer. An inversion scheme compares (in the frequency domain) the experimentally measured data with data predicted using the theoretical model, and an error-function quantifies the difference between these values. Finally, a downhill-simplex algorithm is used to minimize this error-function and thus determine an optimum set of material properties.

Keywords: Plate waves; Laser ultrasonics; Elastic properties

1. Introduction

One important goal of quantitative non-destructive evaluation is the characterization of the material properties of a structural component. The propagation of ultrasonic waves in an elastic medium is an excellent method to gain detailed information about a component's material properties. Wave propagation in layered media provides the fundamental theoretical model for applications such as the characterization of pavements and thin coatings. This is especially true when component parameters such as layer thickness and layer elastic properties are to be determined. Since the elastic constants (and density) are related to the velocity of ultrasonic waves in a medium, the shear and longitudinal bulk wave speeds characterize the elastic properties of the material. In addition, a suitable inversion method must be established to predict the material properties by comparing experimental measurements with a theoretical model.

The objective of the current research is to establish a near field methodology to measure the material properties of a layered media. The unknown properties are determined by comparing measured experimental data with values obtained through numerical simulation. Emphasis is placed on the effectiveness of measuring both the in-plane, and the out-of-plane surface displacement components with a laser Doppler vibrometer (LDV). A theoretical model is used that describes the wave propagation in a homogeneous, linear elastic, infinite layer. The desired material constants are then determined by comparing experimentally measured data with data obtained using the theoretical model. An error-function is set up to quantify the difference between measured and numerically simulated data. A minimization of this error-function with a suitable optimization algorithm results in optimal values for the material properties.

In the near field, there are a limited number of reflections, so the waveform (which is a superposition of evanescent and progressive modes) is not dispersive. Zhou and Popovics [1] used generalized ray theory to theoretically describe wave motion from a point source in the near field; generalized ray theory tracks the motion associated with each possible ray. Weaver et al. [2] developed a theoretical model for the propagation of transient waves in a viscoelastic layer based

* Corresponding author. Tel.: +1-404-894-2771; fax: +1-404-894-0211.
E-mail address: ljacobs@ce.gatech.edu (L.J. Jacobs).
[1] Current address: Institut für Strahlwerkzeuge, Universität Stuttgart, Germany.

0963-8695/03/$ - see front matter © 2003 Elsevier Ltd. All rights reserved.
doi:10.1016/S0963-8695(03)00049-5

on a Hankel transform solution of the viscoelastic wave equations, and compared them with synthetic data to extract phase velocity and attenuation information. The current study develops an analytical solution to the partial differential equations in a double transformed space using a Fourier and a Hankel transformation. In addition, this research considers a driving force that is distributed over a circular area.

The inversion procedure to obtain the material properties minimizes the difference between the theoretical model and experimental measurements. This difference is quantified as an error-function of several variables, and minimized with the downhill-simplex algorithm [3]. Instead of comparing the model with the experimental results in the time domain (as is done in [1]), this study makes the comparison in the frequency domain. Kinra et al. [4] used leaky longitudinal waves to measure thickness and longitudinal wave speed, performing the inversion in the frequency domain. Wu and Liu [5] used surface waves to determine the material properties and the thickness of a bond layer. Ma et al. [6] recently developed a two step inversion procedure for the material properties of a thin-layer that depends on an accurate model of their input source, a pencil lead break.

2. Theoretical model

The theoretical solution for the propagation of ultrasonic waves in a layer is needed as a predictive model for comparison with the experimental measurements. These experimental measurements are made at the surface of the layer, so it is sufficient to have a theoretical model that describes the surface motion. The layer used in this study has a thickness of L and ultrasonic waves are generated by subjecting the top of the layer to a normal, uniformly distributed load of magnitude F_0. The load is applied across a circular area with diameter $2a$ as shown in Fig. 1.

The governing equations are developed using the same notation that Graff [7] uses for a transient normal load on a half space. It is advantageous to formulate these equations in a double transformed space, either as a combination of a Laplace and a Hankel transform (like [7]) or a Fourier transform followed by a Hankel transform, as in this study (see Stolzenburg [8] for details). The radial symmetry with respect to the z-axis calls for a solution in cylindrical coordinates and enables a reduction in unknowns—the circumferential displacement component u_θ is zero and the other two displacement components are independent of θ. The displacement field is expressed using a scalar potential Φ and a vector potential $\vec{H}$, or

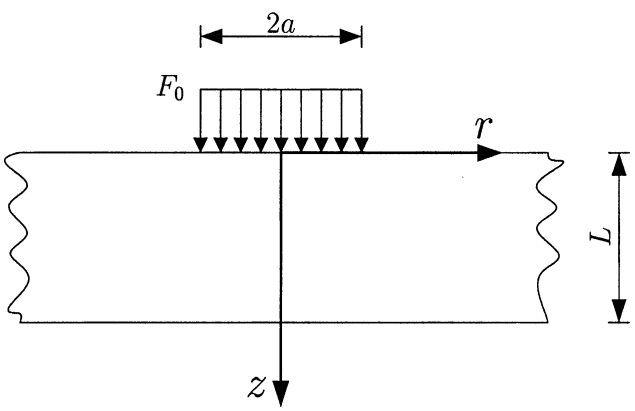

Fig. 1. Sketch of the layer, coordinate system and load.

$$\vec{u} = \nabla\Phi + \nabla \times (H_\theta \vec{e}_\theta) \tag{1}$$

where H_θ is the θ-component of the vector potential $\vec{H}$. Substitution of Eq. (1) into the governing equations of motion (plus the simplifying relationship $H_\theta = -\partial\Psi/\partial r$) leads to two uncoupled partial differential equations in terms of Φ and Ψ and the longitudinal and shear wave speeds, c_L and c_S. These uncoupled governing equations are transformed from the time domain to the frequency domain using a Fourier transform, and then a time harmonic solution (with radial frequency ω) is assumed, leading to the Helmholtz governing equations

$$\nabla^2\tilde{\Phi} + k_L^2\tilde{\Phi} = 0 \qquad \nabla^2\tilde{\Psi} + k_S^2\tilde{\Psi} = 0 \tag{2}$$

where k_L and k_S are the wavenumbers of the longitudinal and shear waves, respectively ($k_L = \omega/c_L$ and $k_S = \omega/c_S$), and ~ denotes a variable in the Fourier transform space.

The Helmholtz governing equations, Eq. (2), are solved using a Hankel transform.

Define a Hankel transform of the n-th order as

$$\bar{f}_n(\xi) = H_n\{\tilde{f}(r)\} = \int_0^\infty r\tilde{f}(r)J_n(r\xi)\,\mathrm{d}r \tag{3}$$

where J_n is the Bessel function of order n, and – denotes a variable in the double transformed (Fourier and Hankel) space. The inverse Hankel transform is given by

$$\tilde{f}(r) = H_n^{-1}\{\bar{f}_n(\xi)\} = \int_0^\infty \xi\bar{f}_n(\xi)J_n(r\xi)\,\mathrm{d}\xi. \tag{4}$$

The Hankel transform of 0-th order is now applied to Eq. (2), resulting in

$$\frac{\mathrm{d}^2\bar{\Phi}}{\mathrm{d}z^2} = \alpha^2\bar{\Phi} \qquad \frac{\mathrm{d}^2\bar{\Psi}}{\mathrm{d}z^2} = \beta^2\bar{\Psi} \tag{5}$$

where

$$\alpha = \sqrt{\xi^2 - k_L^2} \qquad \beta = \sqrt{\xi^2 - k_S^2}. \tag{6}$$

The essential displacement and stress components are now written in the double transformed (Fourier and then Hankel) space. These displacement components are needed for comparison with the experimental results (and the associated inversion), while the stress components are needed to write the relevant boundary conditions. The first order Hankel transform of the Fourier transformed radial displacement is expressed as

$$\bar{u}_r = -\xi(\bar{\Phi} + \bar{\Psi}') \tag{7}$$

where the prime denotes a derivative with respect to z, and the property

$$H_1\left\{\frac{\mathrm{d}\tilde{f}}{\mathrm{d}r}\right\} = -\xi H_0\{\tilde{f}\} \tag{8}$$

presented in Debnath [9] is used. The 0-th order Hankel transform of the out-of-plane displacement is

$$\bar{u}_z = \bar{\Phi}' + \bar{\Psi}'' + k_S^2\bar{\Psi}. \tag{9}$$

The Hankel transform of 0-th order of the stress component $\tilde{\tau}_{zz}$ is written as

$$\tilde{\tau}_{zz} = -\lambda k_L^2\bar{\Phi} + 2\mu(\bar{\Phi}'' + \bar{\Psi}''' + k_S^2\bar{\Psi}'), \tag{10}$$

where λ and μ are the Lamé constants, and using [9]

$$H_0\left\{\frac{1}{r}\frac{\mathrm{d}}{\mathrm{d}r}\left(r\frac{\mathrm{d}\tilde{f}}{\mathrm{d}r}\right)\right\} = -\xi^2 H_0\{\tilde{f}\}. \tag{11}$$

Finally, $\tilde{\tau}_{rz}$ is transformed with a 1-st order Hankel transform as

$$\tilde{\tau}_{rz} = -\mu\xi(2\bar{\Phi}' + 2\bar{\Psi}'' + k_S^2\bar{\Psi}). \tag{12}$$

Next consider the boundary conditions shown in Fig. 1. The only non-zero stress boundary condition (and thus the only value that needs to be transformed) is τ_{zz} at $z = 0$. Without loss of generality, take the amplitude $F_0 = 1$ and this component of stress is double transformed (Fourier and then Hankel) as

$$\bar{F} = \frac{a}{\xi}J_1(a\xi). \tag{13}$$

Note that the other three boundary conditions shown in Fig. 1 are stress free top and bottom of the layer, or in the double transformed space the four transformed boundary conditions are: $\bar{\tau}_{rz} = 0$ at $z = 0$ and $z = L$, $\bar{\tau}_{zz} = 0$ at $z = L$, and $\bar{\tau}_{zz} = aJ_1(a\xi)/\xi$ at $z = 0$.

Assume a solution for the two potentials, $\bar{\Phi}$ and $\bar{\Psi}$, in the form [8]

$$\bar{\Phi} = A_1\,\mathrm{e}^{-\alpha z} + B_1\,\mathrm{e}^{\alpha z} \tag{14}$$

$$\bar{\Psi} = A_2\,\mathrm{e}^{-\beta z} + B_2\,\mathrm{e}^{\beta z}$$

where A_1, A_2, B_1 and B_2 are complex constants that are determined using the four stress boundary conditions just described. The result is a set of four linear equations for the four complex constants; these four equations are shown in Appendix A, Eqs. (24)–(27).

Closed form solutions (in the double transformed domain) are now obtained in terms of modified parameters, $\alpha' = \mathrm{i}\,\alpha = \sqrt{k_L^2 - \xi^2}$ and $\beta' = \mathrm{i}\,\beta = \sqrt{k_S^2 - \xi^2}$. The solution for the two relevant displacements components at $z = 0$ in the double transformed space are

$$\bar{u}_z = \frac{a}{\mu}\frac{i(\xi^2 c_1 - \alpha)\left[(2\xi^2 - k_S^2)\sin(\beta' L)d_1 - 2\alpha\sin(\alpha' L)d_2\right]}{c_2\left[(2\xi^2 - k_S^2)d_2 - 2\beta\xi^2 d_1\right]} \times \frac{J_1(a\xi)}{\xi} \tag{15}$$

$$\bar{u}_r = -\frac{a}{\mu}\frac{\xi(d_2 - \beta d_1)}{(2\xi^2 - k_S^2)d_2 - 2\beta\xi^2 d_1}\frac{J_1(a\xi)}{\xi} \tag{16}$$

with c_1, c_2, d_1 and d_2 given in Appendix A, Eqs. (28)–(31).

Eqs. (15) and (16) are evaluated numerically for different values of ξ. It is seen that for a large values of ξ, the numerical values of sine and cosine terms become very large—larger than the upper limit of a typical numerical program like MATLAB. This upper limit depends on the number of bits used to store a variable. These numerical difficulties are overcome with an asymptotic expression for the displacements in Eqs. (15) and (16) for large values of ξ; express the sine and cosine functions in Eqs. (15) and (16) as exponential functions, and then use asymptotic approximations for these functions. Note that ξ appears in the variables α' and β'. The complex number α' can be written as $\alpha' = \sqrt{k_L^2 - \xi^2} = \delta_\alpha - N_\alpha\mathrm{i}$. For large values of ξ, the magnitude of N_α is much larger than the magnitude of δ_α and both of these numbers are positive. Then asymptotic expressions for the trigonometric functions are

$$\cos(\alpha' L) = \frac{1}{2}\left[\mathrm{e}^{\mathrm{i}\alpha' L} + \mathrm{e}^{-\mathrm{i}\alpha' L}\right] \approx \frac{1}{2}\mathrm{e}^{(\mathrm{i}\delta_{\alpha'} + N_{\alpha'})L} = \frac{1}{2}\mathrm{e}^{\mathrm{i}\alpha' L} \tag{17}$$

$$\sin(\alpha' L) = \frac{1}{2\mathrm{i}}\left[\mathrm{e}^{\mathrm{i}\alpha' L} - \mathrm{e}^{-\mathrm{i}\alpha' L}\right] \approx \frac{1}{2\mathrm{i}}\mathrm{e}^{(\mathrm{i}\delta_{\alpha'} + N_{\alpha'})L} = \frac{1}{2\mathrm{i}}\mathrm{e}^{\mathrm{i}\alpha' L}.$$

The approximation for β' is found in a similar fashion

$$\cos(\beta' L) \approx \frac{1}{2}\mathrm{e}^{\mathrm{i}\beta' L} \qquad \sin(\beta' L) \approx \frac{1}{2\mathrm{i}}\mathrm{e}^{\mathrm{i}\beta' L}. \tag{18}$$

When the above asymptotic expressions are substituted into Eqs. (15) and (16), it is found that the large exponential terms $\mathrm{e}^{\mathrm{i}\alpha' L}\ldots\mathrm{e}^{\mathrm{i}\beta' L}$, in the numerator and denominator of $\bar{u}_z$ and $\bar{u}_r$ cancel out. The asymptotic expressions for $\bar{u}_z$ and $\bar{u}_r$ are written as

$$\bar{u}_z^{(a)} = \frac{a}{\mu}\frac{(\xi^2 c_1 - \alpha)\hat{d}_2}{(2\xi^2 - k_S^2)\hat{d}_2 - 2\alpha\beta\xi^2\hat{d}_1}\frac{J_1(a\xi)}{\xi} \tag{19}$$

$$\bar{u}_r^{(a)} = -\frac{a}{\mu}\frac{\xi(\hat{d}_2 - \alpha\beta\hat{d}_1)}{(2\xi^2 - k_S^2)\hat{d}_2 - 2\alpha\beta\xi^2\hat{d}_1}\frac{J_1(a\xi)}{\xi} \tag{20}$$

with $\hat{d}_1 = \frac{1}{2}(2\xi^2 - k_S^2) - \beta\xi^2 c_1$, and $\hat{d}_2 = \frac{1}{4}(2\xi^2 - k_S^2)^2 - \alpha\beta\xi^2$. There are no terms of $\bar{u}_z^{(a)}$ and $\bar{u}_r^{(a)}$ which exceed the upper limit of MATLAB. A comparison of the asymptotic displacements in Eqs. (19) and (20) with the non-asymptotic displacements in Eqs. (15) and (16) shows that the corresponding expressions approach each other for values of $\xi \approx 1$, and the difference between them converges to zero for larger values of ξ. As a result, the asymptotic

formulation is a good approximation for larger values of ξ [8].

Frequency domain solutions for the displacement components are obtained using an inverse Hankel transform. The out-of-plane displacement in the frequency domain is

$$\tilde{u}_z = \int_0^\infty \bar{u}_z(\xi, z)\xi J_0(r\xi)\mathrm{d}\xi \tag{21}$$

and the in-plane displacement in the frequency domain is

$$\tilde{u}_r = \int_0^\infty \bar{u}_r(\xi, z)\xi J_0(r\xi)\mathrm{d}\xi. \tag{22}$$

These equations enable the calculation of the Fourier-component at a specific frequency. These Fourier-components of the surface displacement components are needed for comparison with the experimental results and for the associated inversion. If the entire transient (time domain) signal is needed, an inverse Fourier transform has to be performed on the entire signal in the frequency domain. Note that the theoretical Fourier-components are calculated with Eqs. (21) and (22) (kernel from Eqs. (15) and (16)), unless the argument in the trigonometric functions exceeds a limit of 150 (above which would cause a numerical error in MATLAB), in which case the asymptotic expressions (Eqs. (19) and (20)) are used to calculate the kernels, $\bar{u}_r$ and $\bar{u}_z$. The integrals in Eqs. (21) and (22) are evaluated numerically using Simpson-1/3 rule, and the number of sample points and the range of integration are selected based on an examination of plots of the integrands. The final choices are checked by doubling the number of integration points and verifying that this does not change the calculated values of the integrals.

Note that the integral expressions in Eqs. (21) and (22) for the harmonic displacements $\tilde{u}_z$ and $\tilde{u}_r$ are exact. These expressions apply for both thick layers ($L \geq \lambda$), and for thin layers ($L < \lambda$), where L is the layer thickness. These integral expressions are also valid in both the near field ($r \leq 10L$) and in the far field ($r > 10L$) of the source. However, the integrands oscillate rapidly at values of r in the far field, making direct calculation of the integrals less accurate. As a result, the integrals should be first simplified using the method of stationary phase for large values of r (in the far field); this case is not examined in this research.

3. Experimental procedure

The experimental measurements are made in a sheet of polymethyl methacrylate (PMMA) 11.7 mm thick, length of 1200 mm and width 600 mm. The ultrasonic waves are generated in the center of the sheet and the width and length dimensions are large enough to avoid disturbances from the edge reflections during the time window of interest—the sheet is treated as an infinite layer with a thickness (L) of 11.7 mm. Ultrasonic waves are generated in this PMMA layer with a contact piezoelectric transducer and are detected with a non-contact, LDV. Fig. 2 describes the experimental setup and instrumentation.

The source transducer used in this study consists of a stack of four piezoelectric (ceramic) discs, each with a diameter of 25.4 mm and thickness of 6.35 mm. The discs are polarized along their thickness, and the resonant frequency of the entire stack is 80.7 kHz. The polarization direction of each disc in the stack is alternated so as to produce a larger ultrasonic signal, and electrical contact is made with copper foil that is glued to the discs with a conducting epoxy. A brass rod (square cross section of 25.4, 330 mm in length) is bonded to one side of the stack—the side not in contact with the PMMA layer. This brass rod acts as an 'absorber' (time delay) of the ultrasonic signal that propagates in the opposite direction, thus reducing any multiple reflections in the stack; these reflections would cause multiple source signals in the PMMA layer. Brass is selected to match the impedance of the PZT discs and thus reduce the reflections from the brass-PZT interface. An independent check on the 'absorption' effectiveness of the brass rod (direct contact with a piezoelectric foil sensor) is conducted with excellent results, see [8] for details. The input signal into the transducer is one cycle of a 100 kHz

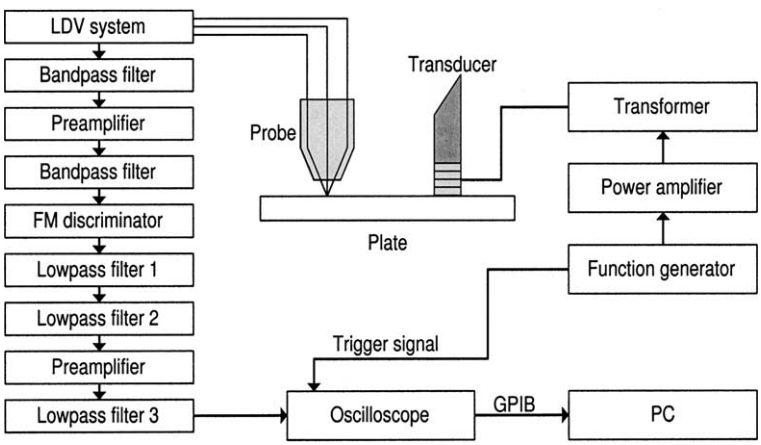

Fig. 2. Experimental setup and instrumentation.

sine wave, with a peak-to-peak amplitude of 750 V. This setup is similar to a commercial piezoelectric shaker, and produces displacement signals on the order of a few nanometers. Note that the minimum detectable particle displacement of the LDV is on the order of tenths of a nanometer.

The LDV used in this research is a heterodyne system capable of making both in-plane and out-of-plane measurements of surface velocity (particle velocity). A general summary of the operation of a similar LDV is available in [10], and a detailed description of the LDV system used in this research is contained in [8]. In brief, this LDV uses an acousto-optic modulator (AOM) to split the incident beam into several, frequency shifted beams that are launched into (polarization preserving) optical fibers. An advantage of the optical fibers is that the detecting probe is independent of the optical bench; this separation results in an LDV that can easily scan a specimen's surface. An additional feature of this LDV system is the use of graded-index cylindrical lenses (GRIN) as transmitting and collection optics. The in-plane configuration uses light reflected from the interference of two incident beams, while the out-of-plane system uses the reflected light from a single incident beam, which is compared with a reference signal. Frequency shifts (Doppler shifts) are measured with a frequency modulation (FM) discriminator. A mechanical shutter is used to change the system from the in-plane to the out-of-plane configuration. This LDV makes high-fidelity, absolute, non-contact measurements over a frequency bandwidth of 10 kHz–10 MHz. Note that all signals are amplified and are bandpass filtered between 3 and 300 kHz. In addition, each signal is averaged 2000 times to reduce noise.

4. Experimental results and inversion

First consider an out-of-plane time domain signal measured in the PMMA layer with a propagation distance (source-to-receiver distance), r, equal to 25 mm. Fig. 3 compares this experimentally measured (transient) signal with the theoretically predicted signal calculated with an inverse fast Fourier transform (FFT) of Eq. (21), plus the predicted out-of-plane displacement calculated using the results of [2]. Note that both theoretical models correctly predict the positions of the peaks, but the model using Eq. (21) is more accurate in describing the height of the peaks. Both theoretical solutions should be equivalent, so any differences are due to numerical errors; it appears that Eq. (21) is less sensitive to numerical error than the theoretical solution presented in [2]. The inversion procedure uses only a selected Fourier component of the experimentally measured signal (this procedure is described in detail later). However, the comparison of the measured and predicted transient signals (Fig. 3) is a useful check of both the accuracy of the experimental procedure and the theoretical model. Note that the transient drive force is assumed to be proportional to the voltage applied to the drive transducer, and that handbook values are assumed for c_L and c_S.

Next, surface motion (both in-plane and out-of-plane) is measured at nine different source-to-receiver distances, varying from 35 to 75 mm (with a step size of 5 mm). Repeatability of the inversion process is ensured by taking two sets of data at each location. The Fourier-components of these nine experimentally measured time domain, ultrasonic signals are obtained (at the drive frequency, 100 kHz) with an FFT of the entire signal.

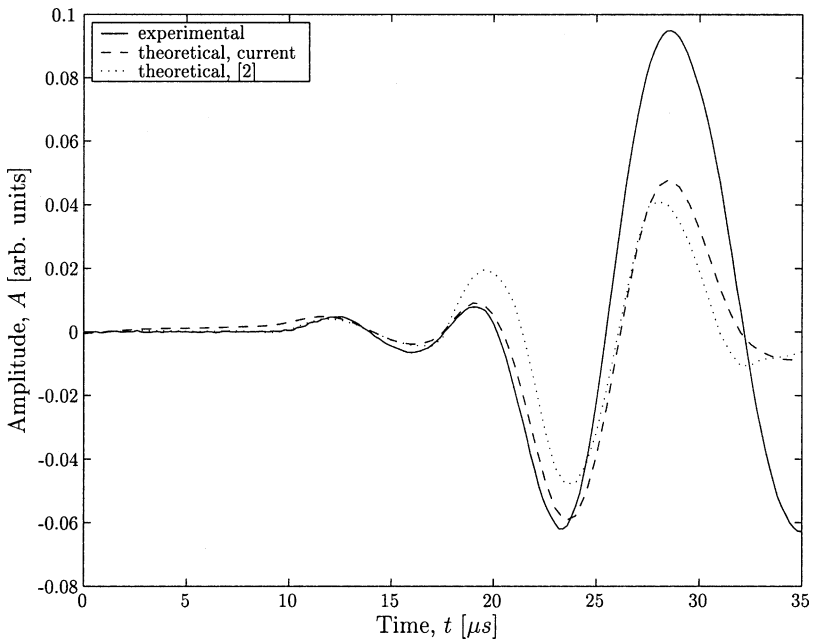

Fig. 3. Comparison of time domain (out-of-plane) experimental results with two theoretical models.

An error-function, ϵ, is now developed to quantitatively describe how well the theoretical model matches the experimentally measured data. Consider the Fourier-components of five different ultrasonic signals (at the drive frequency, 100 kHz), each having a different source-to receiver distance, r. This yields five pairs of theoretical amplitudes and phases $(A_i)_{\text{th}}$ and $(\phi_i)_{\text{th}}$, as well as five experimental (measured) pairs, $(A_i)_m$ and $(\phi_i)_m$. Note $i = 1, 2 \ldots 5$, the subscript m denotes experimentally measured data, while the subscript th denotes values calculated from the theoretical model. The amplitudes are normalized by dividing by A_1, while the phases are normalized by subtracting ϕ_1. Define the error-function as

$$\epsilon = \sum_{i=2}^{5} \left[\left(\frac{A_i}{A_1} \right)_m - \left(\frac{A_i}{A_1} \right)_{\text{th}} \right]^2 + \sum_{i=2}^{5} \left[(\phi_i - \phi_1)_m - (\phi_i - \phi_1)_{\text{th}} \right]^2. \quad (23)$$

This error-function can be calculated individually for each component of displacement, or combined as $\epsilon_{rz} = \epsilon_r + \epsilon_z$, where ϵ_r is the error-function calculated from the in-plane motion, ϵ_z is the error in the out-of-plane motion, and ϵ_{rz} is the combined error-function.

Consider an error-function in terms of two unknowns, the longitudinal and shear wave speeds. The in-plane error-function, ϵ_r, is shown in Fig. 4, while the out-of-plane error-function, ϵ_z, is shown in Fig. 5. Fig. 4 has a single absolute minimum, plus several sharp peaks away from this minimum. Note the existence of two local minima close to the sharp peaks that are marked with arrows. These local minima complicate the convergence of any algorithm used for the minimization procedure. In contrast, ϵ_z (shown in Fig. 5) does not have any local minima or sharp peaks, but instead has a single minimum—the existence of this single minimum will simplify convergence of the minimization. Note that the absolute minima for both ϵ_r and ϵ_z are very close to each other. It is also clear that the values of ϵ_r are several orders of magnitude larger than ϵ_z (the ϵ-axis is logarithmic in both figures), so the combined error-function, ϵ_{rz}, is dominated by ϵ_r, showing a similar behavior with several local minima.

The downhill-simplex algorithm [3] is now used to minimize these error-functions, thus obtaining the most accurate (optimum) values for the relevant material properties. The downhill-simplex algorithm is selected because it is capable of minimizing a function of several variables, no derivatives are required for its implementation, and it is efficient in the number of function evaluations required. An initial estimation is required to start the downhill-simplex algorithm, and this estimate is a critical step. If the initial guess is too far from the true values of c_{L} and c_{S}, this algorithm will not coverage. The research uses the following procedure to develop the initial estimate. An examination of the measured transient signals identifies a strong Rayleigh wave component, so this study uses this arrival time to generate a rough estimate of c_{S}. A time-of-flight analysis identifies the arrival of the Rayleigh wave, and a first guess of the shear wave speed is generated with $\frac{c_{\text{R}}}{c_{\text{S}}} \approx 0.9$, where c_{R} is the Rayleigh wave speed. An additional estimation of the longitudinal wave speed is based on an approximate ratio between longitudinal and shear wave speeds—a factor of two for plastics, such as PMMA, in the glassy state [8].

Each of the three error-functions (ϵ_r, ϵ_z and ϵ_{rz}) are minimized. The sharp peaks and local minima in ϵ_r cause

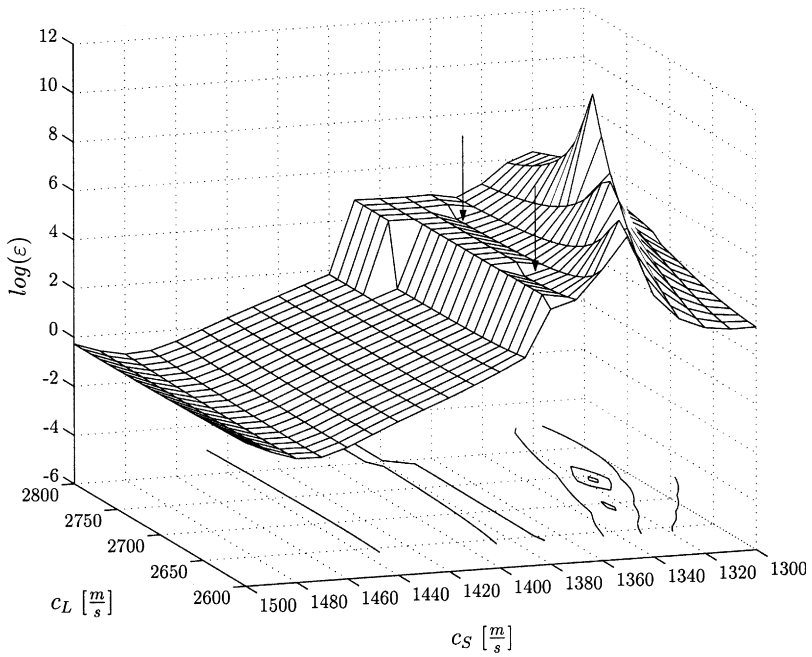

Fig. 4. Error-function for the in-plane measurements, ϵ_r.

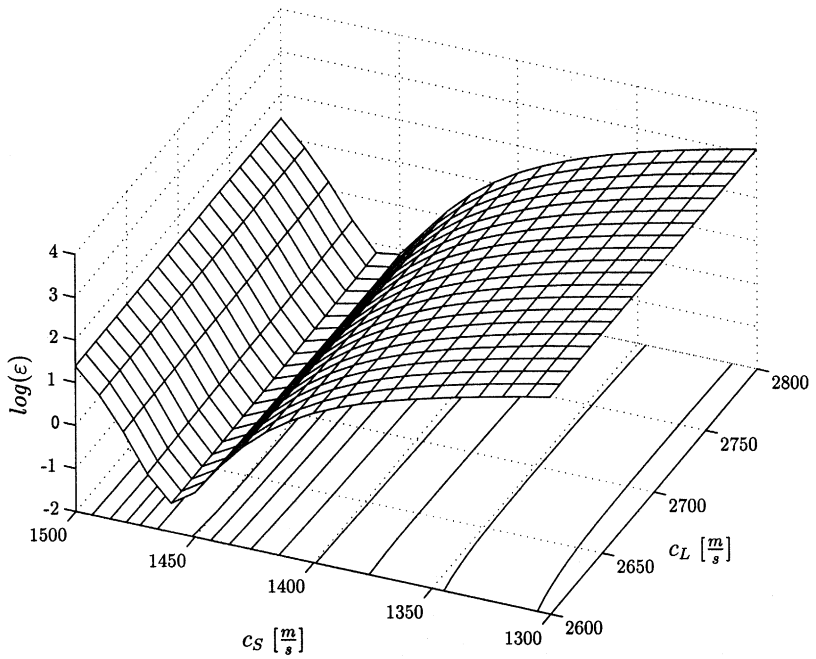

Fig. 5. Error-function for the out-of-plane measurements, ϵ_z.

some complications in its minimization, as well as the minimization of the combined error-function (ϵ_{rz}). Potential problems are alleviated by using the results from the out-of-plane motion, ϵ_z, to start the minimization of the other two error-functions. Fifty iterations are sufficient to achieve convergence of ϵ_z. These optimized values are then multiplied by random factors between 0.95 and 1.05, used as the starting values for the minimization of ϵ_r and ϵ_{rz}, and an additional 50 iterations are needed for convergence. The results of the minimization process for the three error-functions (and for the two sets of experimental data) are shown in Table 1 and the evolution during minimization of the combined error-function (ϵ_{rz}) is shown Fig. 6. A comparison of these results shows that the optimized values of the wave speeds predicted with three different error-functions are all very close to each other, with the largest differences present in the longitudinal wave speed values (note that these differences are very small, on the order of 1%).

It is now interesting to present a comparison between the Fourier-components from the experimentally measured signals and the theoretically predicted data—the theoretical values calculated using the optimized values of c_L and c_S predicted from the end of the downhill-simplex algorithm—at the drive frequency, 100 kHz. Figs. 7 and 8 present the Fourier-components for the in-plane, and out-of-plane displacements, respectively. Figs. 7 and 8 show the amplitude A and phase ϕ for each of the nine propagation distances, and for each of the two sets of measurements. There is excellent agreement between the experimental and theoretical results, demonstrating the accuracy of the theoretical model, the fidelity of the experimental procedure, and the effectiveness of the downhill-simplex algorithm. Figs. 7 and 8 also show that the inversion procedure developed in this study is based on the relative change in amplitude and phase of a single Fourier-component in the measured time domain signal. An advantage of this procedure is that it does not require accurate measurement of the transient force applied to the layer at the source transducer. However, the theoretical model is based on an infinite layer, so it is necessary to window the measured time domain signals (before taking the Fourier transform) to remove the reflections from the layer boundaries.

A statistical analysis is now performed to determine the influence of measurement error on the resulting optimized wave speeds. In brief, the experimentally measured amplitudes and phases are multiplied by random factors between 0.95 and 1.05, which corresponds to an experimental error of $\pm 5\%$. Twenty-five new minimizations are performed, and the mean values ($\bar{x}$) and standard deviations (σ) are compared to identify convergence trends, see Table 2. The statistical scatter in ϵ_{rz} tends to be smaller because it is based on a larger number of measurement points (double). Note that an increase in the number of measurement sets (from the five used in this study) will increase the accuracy of the results, since there will be more

Table 1
Results from inversion for longitudinal and shear wave speeds

Error-function	Measurement set 1			Measurement set 2		
	c_L (m/s)	c_S (m/s)	ϵ	c_L (m/s)	c_S (m/s)	ϵ
ϵ_r	2611.2	1474.2	0.385	2630.9	1466.8	0.237
ϵ_z	2648.1	1458.1	0.289	2647.3	1445.8	0.999
ϵ_{rz}	2645.2	1458.1	0.889	2599.5	1453.9	1.464

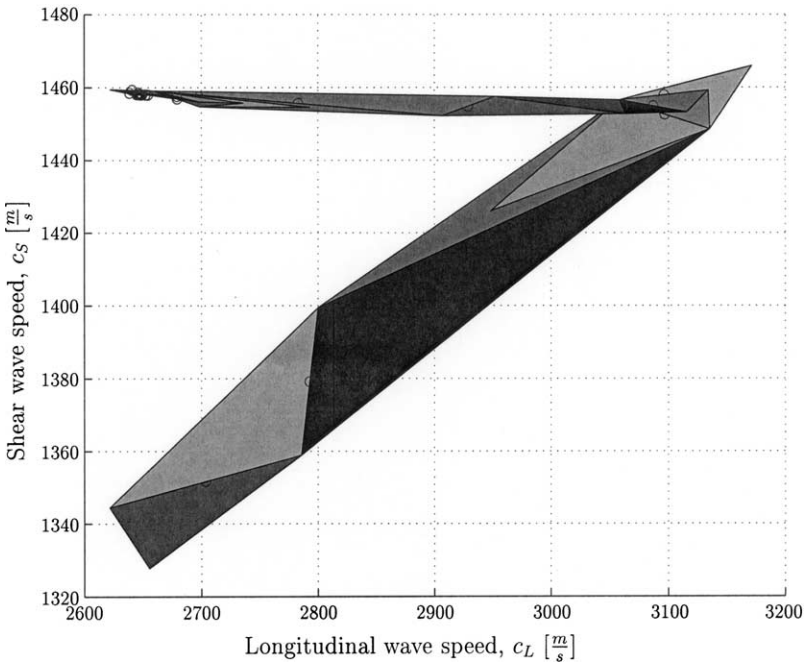

Fig. 6. Convergence of downhill-simplex algorithm in the minimization of the error-function ϵ_{rz}.

averaging of random experimental error. With respect to the sensitivity to measurement errors, ϵ_z performs the best, and the shear wave speed minimization is the most stable and accurate. This simulated random measurement error of $\pm 5\%$ causes a scatter in the shear wave speed predictions below 1%.

Overall, these results demonstrate that the proposed inversion scheme based on five measurement data points leads to excellent results for shear and longitudinal wave speeds, with shear wave speed being slightly superior. Given a choice, ϵ_z is more stable, has better convergence performance, and is less sensitive to the values selected for the initial wave speed approximations. As a result, out-of-plane measurements are more effective than in-plane measurements for this near field inversion.

The values of c_L and c_S in Tables 1 and 2 can also be compared with previously published values for PMMA, such as c_L of 2690–2756 m/s and c_S of 1300–1401 m/s as

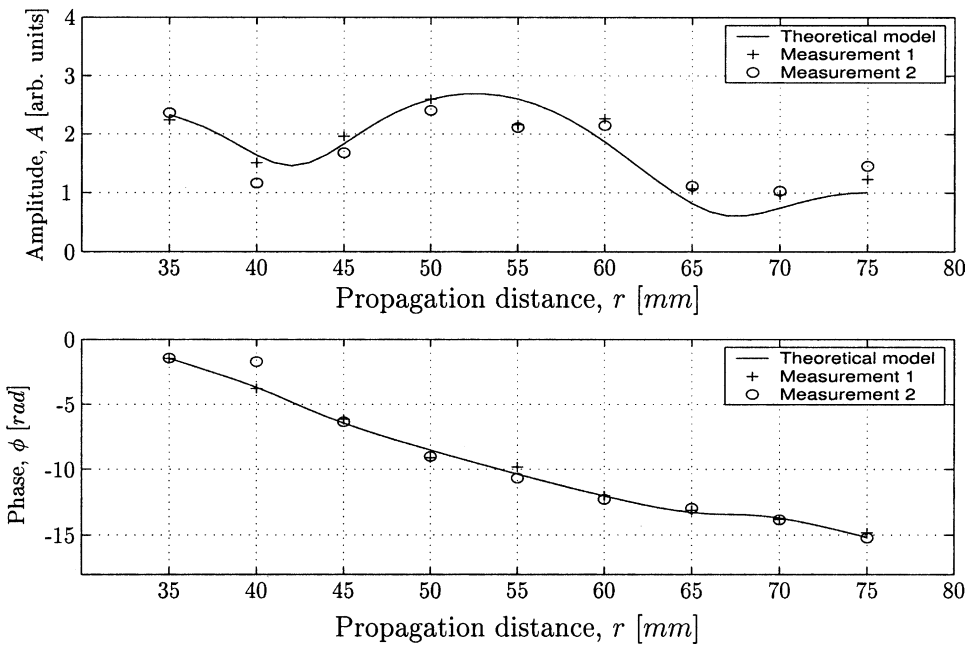

Fig. 7. Fourier-components of the in-plane displacement, comparison of theoretical and experimental.

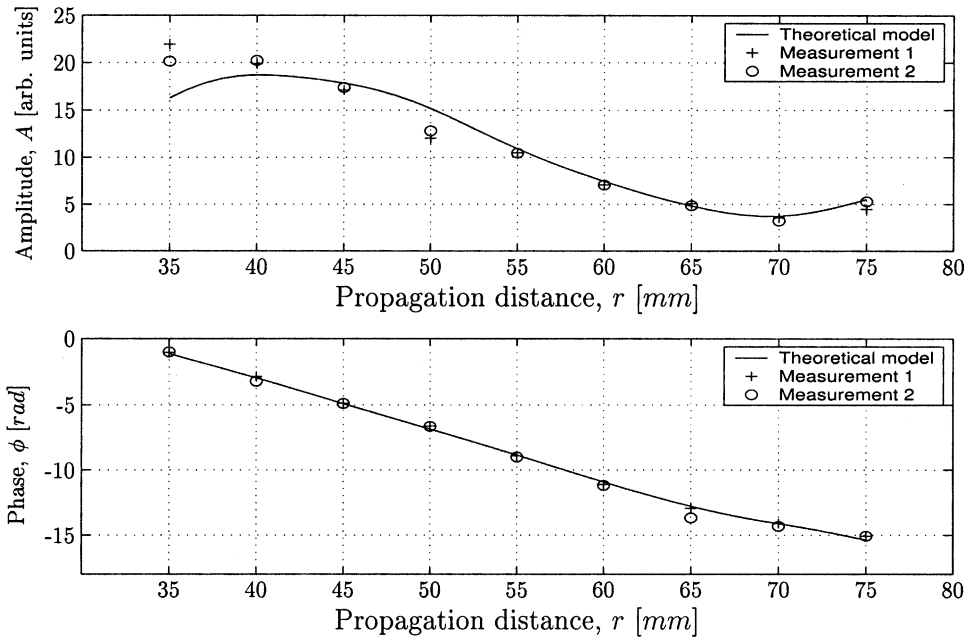

Fig. 8. Fourier-components of the out-of-plane displacement, comparison of theoretical and experimental.

determined with ultrasonic time-of-flight measurements [11]. Note that the measurements in [11] were not in situ, and required samples of a specified size and shape. The variability in previously published values is partly due to errors in the measurement technique, and partly due to batch-to-batch variations in PMMA.

Now consider layer thickness, L, as a third unknown. The initial estimation for the wave speeds and thickness is critical for the success of this minimization. Take a thickness estimation that is based on the results from the previously described inversion for two unknowns (longitudinal and shear wave speeds), and treating the layer thickness as the single unknown. The resulting error-functions (all for one unknown, L) are minimized for thickness, L, and this value of thickness is used as the initial estimation in the inversions for the three unknowns. Minimization of the three unknown error-functions is accomplished with a three-dimensional downhill-simplex algorithm, and the results (after 150 iterations) are presented in Table 3—the results for the error-functions ϵ_r and ϵ_{rz} are very accurate. The optimized wave speeds are close to the solutions obtained with the minimization for the two wave speeds (Table 1) and the calculated thickness is close to the actual layer thickness of 11.7 mm. The best results are obtained with the combined error-function (ϵ_{rz}). In contrast, the out-of-plane error-function, ϵ_z, is inconsistent in its prediction of longitudinal wave speed, where the algorithm converges to values far away from the actual values. The reason for the large error in longitudinal wave speed in the ϵ_z predictions is the small slope of ϵ_z in the c_L-direction, making this inversion very sensitive to measurement error. Clearly the error-function ϵ_z is not a suitable choice to determine all three material properties.

A statistical analysis is performed on ϵ_r and ϵ_{rz}, again using 25 minimizations with a random error of $\pm 5\%$. The results are shown in Tables 4 and 5 and compared to

Table 2
Effect of measurement errors on first inversion

Error-function	$\bar{x}(c_L)$ (m/s)	$\bar{x}(c_S)$ (m/s)	$\sigma(c_L)$ (m/s)	$\sigma(c_S)$ (m/s)
Measurement set 1				
ϵ_r	2733.2	1479.0	225.41	15.05
ϵ_z	2670.1	1460.5	177.63	9.87
ϵ_{rz}	2640.6	1465.0	80.56	5.99
Measurement set 2				
ϵ_r	2770.7	1471.2	310.3	14.25
ϵ_z	2673.1	1446.5	77.15	9.48
ϵ_{rz}	2642.1	1455.0	109.92	5.08

Table 3
Results from inversion for longitudinal and shear wave speeds, plus thickness

Error-function	c_L (m/s)	c_S (m/s)	L (mm)	ϵ
Measurement set 1				
ϵ_r	2696.6	1511.0	12.02	0.198
ϵ_z	5979.9	1396.2	11.09	0.177
ϵ_{rz}	2625.1	1472.2	11.77	0.786
Measurement set 2				
ϵ_r	2715.6	1449.3	11.54	0.167
ϵ_z	3367.5	1390.9	11.22	0.742
ϵ_{rz}	2690.0	1425.8	11.45	1.216

Table 4
Mean values for second inversion with measurement error

Error-function	$\bar{x}(c_L)$ (m/s)	$\bar{x}(c_S)$ (m/s)	$\bar{x}(L)$ (mm)
Measurement set 1			
ϵ_r	2697.9	1505.3	11.95
ϵ_{rz}	2624.5	1473.2	11.77
Measurement set 2			
ϵ_r	2772.0	1455.4	11.58
ϵ_{rz}	2740.0	1423.7	11.45

Table 5
Standard deviations for second inversion with measurement error

Error-function	$\sigma(c_L)$ (m/s)	$\sigma(c_S)$ (m/s)	$\sigma(L)$ (mm)
Measurement set 1			
ϵ_r	118.61	32.00	0.245
ϵ_{rz}	57.52	23.38	0.174
Measurement set 2			
ϵ_r	219.06	26.81	0.221
ϵ_{rz}	159.07	17.17	0.134

the results in Table 2, the standard deviation for shear wave speed has increased, while there are no major changes in the longitudinal wave speed values. The standard deviation for thickness is below 2%. The proposed inversion scheme is clearly capable of accurately determining both shear and longitudinal waves speeds, as well as layer thickness.

5. Conclusion

The study develops an in situ methodology using ultrasonic waves to measure the material properties and thickness of a layer. Wave motion in the near field is described by a theoretical model in a double transformed space. The theoretical model accurately predicts the surface displacement of a layer in both the time and frequency domains. The experimental procedure uses an LDV to make (nearly) simultaneous measurements of in-plane and out-of-plane surface displacement components. An inversion scheme is developed that compares the experimentally measured data with data predicted using the theoretical model in the frequency domain. An error-function quantifies the difference between these values, and a downhill-simplex algorithm is used to minimize this error-function and thus determine an optimum set of material properties.

The proposed comparison in the frequency domain is shown to be computationally efficient, and the error-functions (based on amplitude and phase information from the drive Fourier-component) show a single, distinct absolute minimum. If the only material properties of interest are the longitudinal and shear wave speeds, an inversion of the out-of-plane displacements gives the best results. This inversion is very robust, especially for the shear wave velocity. In contrast, if an inversion for the layer thickness, plus longitudinal and shear wave speeds is desired, the best results are obtained with an error-function based on the in-plane surface motion.

Acknowledgements

The Deutscher Akademischer Austausch Dienst (DAAD) provided partial support to Christian Stolzenburg.

Appendix A

The four linear equations for the double transformed boundary conditions are

$$(-\lambda k_L^2 + 2\mu\alpha^2)A_1 + (-2\mu\beta^3 - 2\mu k_S^2\beta)A_2 + (-\lambda k_L^2 + 2\mu\alpha^2)B_1 + (2\mu\beta^3 + 2\mu k_S^2\beta)B_2 = \frac{a}{\xi}J_1(a\xi) \tag{24}$$

$$(-2\alpha)A_1 + (2\beta^2 + k_S^2)A_2 + (2\alpha)B_1 + (2\beta_2 + k_S^2)B_2 = 0 \tag{25}$$

$$(-\lambda k_L^2 + 2\mu\alpha^2)e^{-\alpha L}A_1 + (-2\mu\beta^3 - 2\mu k_S^2\beta)e^{-\beta L}A_2 + (-\lambda k_L^2 + 2\mu\alpha^2)e^{\alpha L}B_1 + (2\mu\beta^3 + 2\mu k_S^2\beta)e^{\beta L}B_2 = 0 \tag{26}$$

$$(-2\alpha)e^{-\alpha L}A_1 + (2\beta^2 + k_S^2)e^{-\beta L}A_2 + (2\alpha)e^{\alpha L}B_1 + (2\beta_2 + k_S^2)e^{\beta L}B_2 = 0. \tag{27}$$

The four coefficients used in Eqs. (15) and (16) are

$$c_1 = \frac{2\alpha}{2\xi^2 - k_S^2} \tag{28}$$

$$c_2 = 2\alpha\{\cos(\beta' L) - \cos(\alpha' L)\} \tag{29}$$

$$d_1 = 2\alpha(2\xi^2 - k_S^2)[\cos(\alpha' L)\cos(\beta' L) - 1] + 4\alpha\beta\xi^2 c_1 \sin(\alpha' L)\sin(\beta' L) \tag{30}$$

$$d_2 = 4\alpha\beta\xi^2[1 - \cos(\alpha' L)\cos(\beta' L)] - (2\xi^2 - k_S^2)^2\sin(\alpha' L)\sin(\beta' L). \tag{31}$$

References

[1] Zhou C, Popovics J. Point load wave excitation in multi-layered: solids: experiments and model verification. J Acoust Soc Am 2001; 109(5):1838–40.
[2] Weaver RL, Sachse W, Niu L. Transient ultrasonic waves in a viscoelastic plate: theory. J Acoust Soc Am 1989;85(6): 2255–61.
[3] Nelder JA, Mead R. A simplex method for function minimization. Comput J 1965;7:308–13.

[4] Kinra VK, Jaminet PT, Zhu C, Iyer VR. Simultaneous measurement of the acoustical properties of a thin-layered medium: the inverse problem. J Acoust Soc Am 1994;95(6):3059–74.
[5] Wu TT, Liu YH. Inverse determination of thickness and elastic properties of a bonding layer using laser-generated surface waves. Ultrasonics 1999;37:23–30.
[6] Ma CC, Liu SW, Chang CM. Inverse calculation of material parameters for a thin-layer system using transient elastic waves. J Acoust Soc Am 2002;112(3):811–21.
[7] Graff KF. Wave motion in elastic solids. New York: Dover Publications; 1991.
[8] Stolzenburg JC. Non-contact method to measure the material properties of layered media. MS Thesis, Engineering Science and Mechanics, Georgia Institute of Technology, Atlanta, GA; 2001.
[9] Debnath L. Integral transforms and their applications. Boca Raton, Florida: CRC Press; 1995.
[10] Kil HG, Jarzynski J, Berthelot YH. Wave decomposition of the vibrations of a cylindrical shell with an automated scanning laser vibrometer. J Acoust Soc Am 1994;95(6):3059–74.
[11] Hartmann B, Jarzynski J. Immersion apparatus for ultrasonic measurements in polymers. J Acoust Soc Am 1974;56(5):1469–77.